

Supervised Learning Enhanced by an Entangled Sensor Network

Quntao Zhuang^{1,2*} and Zheshen Zhang^{3,4}

¹*Department of Electrical and Computer Engineering,
University of Arizona, Tucson, Arizona 85721, USA*

²*Department of Physics, University of California, Berkeley, California 94720, USA*

³*Department of Materials Science and Engineering,
University of Arizona, Tucson, Arizona 85721, USA*

⁴*College of Optical Sciences, University of Arizona, Tucson, AZ 85721, USA*

(Dated: June 11, 2022)

Various existing quantum supervised learning (SL) schemes rely on quantum random access memories to store quantum-encoded data given *a priori* in a classical description. The data acquisition process, however, has not been accounted for, while it sets the ultimate limit of the usefulness of the data for different SL tasks, as constrained by the quantum Cramér-Rao bound. We introduce supervised learning enhanced by an entangled sensor network (SLEEN) as a means to carry out SL tasks at the physical layer where a quantum advantage is achieved. The entanglement shared by different sensors boosts the performance of extracting global features of the object under investigation. We leverage SLEEN to construct an entanglement-enhanced support-vector machine for quantum data classification and entanglement-enhanced principal component analyzer for quantum data compression. In both schemes, variational circuits are employed to seek the optimum entangled probe state and measurement settings to maximize the entanglement-enabled quantum advantage. We compare the performance of SLEEN with separable-state SL schemes and observe an appreciable entanglement-enabled performance gain even in the presence of loss. SLEEN is realizable with available technology, opening a viable route toward building near-term quantum devices that offer unmatched performance beyond what the optimum classical device is able to afford.

Keywords: Quantum Information, Quantum Physics, Optics.

I. INTRODUCTION

While error-corrected scalable quantum computation is not yet available, recent advances towards a small-scale quantum computer [1, 2] have spurred interests in seeking noisy intermediate-scale quantum (NISQ) [3] devices that offer unmatched performance beyond the capability of classical devices. The theoretical proof of a quantum advantage over classical computation [4, 5] further inspires the search for quantum-enhanced schemes tailored for practical tasks. In this regard, quantum variational schemes, in conjunction with classical optimization, are widely applicable to tasks including quantum state preparation [6], variational eigen-solvers [7, 8], state diagonalization [9] and machine learning [10–14].

With respect to quantum machine learning, most algorithms rest upon input data given *a priori* in a classical description. The classical data are subsequently quantum encoded, stored in quantum random access memories (qRAMs), and processed by quantum circuits. The quantum machine learning algorithms aim to efficiently solve certain tasks that are intractable by the optimum classical algorithm. Achieving such a quantum advantage is however held back by various challenges in, e.g., preserving quantum coherence, the efficient construction of qRAMs [15], and a lack of understanding for what noisy quantum circuits would be able to offer.

In this paper, we introduce supervised learning enhanced by an entangled sensor network (SLEEN), a different quantum supervised learning (SL) paradigm that carries out SL tasks and achieves a quantum advantage at the physical layer during the data acquisition process. The SLEEN architecture consists of quantum circuits and an entangled sensor network. Utilizing a variational approach, the quantum circuits optimize the multipartite entangled probe state shared in the sensor network and seek the optimum measurement setting for the optimum capture of the object’s features of interest.

The SLEEN architecture can be employed in two major tasks with quantum advantages, the support-vector machine (SVM) for quantum data classification and principal component analyzer (PCA) for quantum data compression. Different from other quantum SL algorithms, the quantum advantage for SLEEN can be quantified using tools from quantum measurement theory. In a classification task undertaken by M entangled sensor nodes, the error probability of SLEEN $\propto P^M$ is exponentially better than the error probability P of the optimum classical strategy in the absence of loss, and the advantage survives loss. SLEEN can be readily implemented as it only requires off-the-shelf components such as single-mode squeezers, linear optical circuits, and homodyne measurements. It will give rise to an appreciable quantum advantage in SL tasks pertaining to non-demolition detection [16], thermometry [17], radial-frequency (RF) sensing [18], biomolecule sensing [19], and phase estimation [20, 21].

* zhuangquntao@gmail.com

II. THE ARCHITECTURE

In most existing SL schemes, be they classical or quantum, the data given *a priori* are in a classical description. What the existing SL schemes have not accounted for is the data acquisition process, which in general involves measurements on probe states to map the physical properties of interest to their classical descriptions. From a quantum sensing perspective [22–24], data acquisition is modeled as parameter estimation of a channel, i.e., a completely-positive and trace-preserving (CPTP) linear map [25], using a probe state followed by quantum measurements. For instance, in the target-detection scenario illustrated in Fig. 1, interrogating the presence or absence of the target is through using probe states to estimate the transmissivity of a lossy and noisy bosonic channel [26]. Such a generalized data-acquisition picture is also applicable to fluorescence imaging [27, 28], optical reading [29], phase sensing [20, 21, 30], magnetic measurements [31], and fiber optic gyroscopes [32].

The amount of available information, carried on the probe state, about the object under investigation is ultimately dictated by the quantum Cramér-Rao bound [33–35] arising from measurement uncertainties. This sets a fundamental limit for the SL schemes that process data given *a priori* in a classical description, because obtaining a precise classical description of the quantum channels requires an expensive overhead. On the other hand, like classification tasks, most SL tasks only aim to investigate global features of the object, rendering obtaining classical descriptions for local features redundant.

To overcome this overhead, SLEEN carries out SL tasks at the physical layer during the data acquisition process, without resorting to precise knowledge about local features. At the core of the SLEEN architecture is a network of entangled sensors optimized by variational circuits, as illustrated by a target-detection example in Fig. 1. These sensors are distributed at different spatial locations, frequencies, or temporal modes, depending on the object’s features of interest. Each sensor views the object from a different perspective. SLEEN’s quantum advantage is two-fold: (i) the direct measurement of the global information by the variational circuits reduces errors and obviates the overhead in obtaining redundant local information about the target; and (ii) the entanglement shared by different sensors boosts the sensitivity of extracting global information of the object under investigation, thereby leading to a large quantum advantage in SL tasks such as SVM and PCA. The quantum advantage at the physical layer makes SLEEN significantly different from existing quantum SL schemes that require error-corrected quantum circuits and qRAMs to achieve the quantum advantage.

Prior studies [30, 36, 37] on entangled sensor networks show that for the problem of estimating a global parameter of the network, e.g., a weighted sum of phase shifts measured by different sensors, shared entanglement leads to a measurement-sensitivity scaling advantage, i.e., ap-

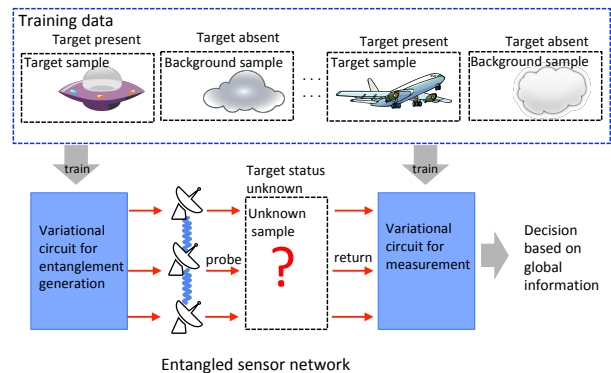


Figure 1. The SLEEN architecture applied to a data classification task in a target-detection scenario. The sensors, represented by the probe icons, share a multipartite entangled probe state. Each sensor sends its share of the entangled probe state to investigate an object. The sensing process is modeled as channel-parameter estimation. Each sensor views the object from a different perspective, and their shared entangled probe state boosts the performance of estimating a global parameter of the object. Prior to interrogating an unknown object, existing data are used to train the first variational circuit (left blue box) to generate the optimum entangled probe state and the second variational circuit (right blue box) to perform the optimum measurement.

proaching the Heisenberg limit [22, 23, 38–41] with respect to the number of sensors, over the optimum unentangled sensor network. In particular, Ref. [30] presents entangled sensor networks based on continuous variables (CVs) and proved that the root-mean-square (rms) estimation error for estimating a weighted sum of displacements at different sensor nodes is a factor of $\sim 1/\sqrt{M}$ smaller than a product-state sensor network, where M is the number of sensor nodes. In addition, Appendix A shows that the measurement-sensitivity advantage in parameter estimation translates to an *exponential* error-probability advantage in channel discrimination.

Entangled sensor networks’ quantum advantage in channel discrimination makes them well suited for SL tasks. To fully unleash the power of the entangled sensor network for different SL tasks, one needs to tailor the entangled probe state shared between the sensor nodes and optimize the measurement setting. For a complex SL task, deriving the optimum entangled probe state and measurement configuration becomes a formidable problem. Take the target-detection problem depicted in Fig. 1 as an example. The target object is embedded in a highly dynamic environment so our goal is to optimize the entangled probe state shared by the sensor nodes and design a measurement strategy to minimize the error probability of interrogating the presence or absence of the target. In the SLEEN architecture, an optical circuit, trained by a variational approach, generates the entangled probe state. Likewise, a second variational optical circuit processes the return entangled probe state prior to the measurement. In doing so, SL tasks are carried

out during the data acquisition process at the physical layer, thereby eliminating the need for precise knowledge about local features. The training data and the variational approach ensure that the quantum advantage is reaped for a variety of SL tasks. Moreover, since CV entangled sensor networks enjoy loss tolerance, deterministic entanglement preparation, and efficient broadband measurements [30], the quantum advantage of SLEEN is realizable with available technology.

III. ENTANGLEMENT-ENHANCED PHYSICAL-LAYER SUPPORT-VECTOR MACHINE

To demonstrate the power of SLEEN, we utilize it to construct an entanglement-enhanced SVM for data classification at the physical layer. As shown in Fig. 2 (top), the SVM structure entails an entangled sensor network that probes an object through the estimation of the parameters of the quantum channel $\Phi^{(n)}$. Channel $\Phi^{(n)}$ imparts M unitary operations, $\hat{U}(\alpha_1^{(n)})$ to $\hat{U}(\alpha_M^{(n)})$, on the probe state represented by M annihilation operators \hat{a}_1 to \hat{a}_M . At present, we assume the channels are lossless, but will later add in pure loss channels with transmissivity η to account for experimental imperfections. Here, we consider displacement unitaries $\hat{U}(\alpha_m^{(n)}) \equiv \exp(-i\alpha_m^{(n)}\hat{p})$, with the understanding that phase shift can be transformed into field displacement by a Mach-Zehnder interferometer (see Appendix C for details), thereby greatly broadening the scope that SLEEN applies to.

In the above scenario, each channel instance is described by a set of displacements, $\alpha^{(n)} = (\alpha_1^{(n)}, \dots, \alpha_M^{(n)})$, in which the features of the object are embedded. The data acquisition process aims to estimate certain information of the channel parameter $\alpha^{(n)}$, while the exact value of $\alpha^{(n)}$ is unknown to the SL tasks. One option is to precisely estimate each component of $\alpha^{(n)}$ with repetitive measurements, and then the problem can be solved by a classical SVM [42]. In this case, a hyperplane described by $\mathbf{w} \in \mathbb{R}^M, b \in \mathbb{R}$ is chosen, and

$$\hat{y}^{(n)} = \text{sign}(\mathbf{w} \cdot \alpha^{(n)} + b) \quad (1)$$

is used to generate a class label. Here, $\text{sign}(\cdot)$ is the sign function. Efficient classical algorithms can be used to optimize the hyperplane from the training data. However, one immediately notice that Eq. 1 only relies on a global quantity $\mathbf{w} \cdot \alpha^{(n)}$ of the channel, thus measuring each component of $\alpha^{(n)}$ is redundant. Moreover, repetitive measurements of the same channel is not only inefficient, but also impossible if each channel is transient and can only be accessed a few times. To resolve this issue, the SLEEN architecture is adopted to perform data classification at the physical layer.

Our goal is to optimize the entangled probe state and

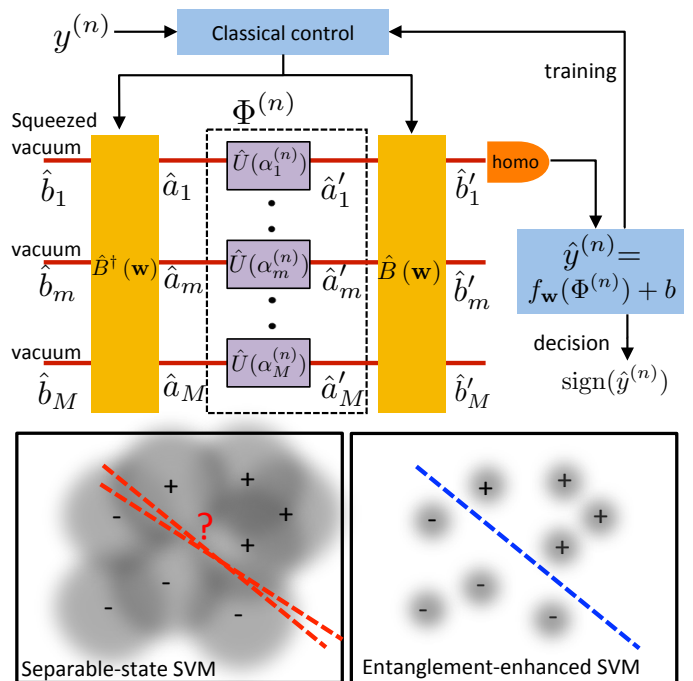


Figure 2. Top panel: schematic of the entanglement-enhanced support-vector machine. Two variational circuits $\hat{B}^\dagger(\mathbf{w})$ and $\hat{B}(\mathbf{w})$ are trained to generate the optimum entangled probe state and to preprocess the quantum state for the optimum measurement. The data are acquired by estimating the parameters of the quantum channel $\Phi^{(n)}$ comprised of M displacement operations parametrized by $\alpha^{(n)} = \{\alpha_1^{(n)}, \dots, \alpha_M^{(n)}\}$. “homo” denotes a homodyne measurement that returns $\hat{y}^{(n)}$ as the measurement outcome. The classical control algorithm uses the simultaneous perturbation stochastic approximation (SPSA) method to update the setting \mathbf{w} for the variational circuits. Bottom panels: illustration of the performance contrast between the entanglement-enhanced SVM and separable-state SVM in the parameter space. The labels ‘+’ and ‘-’ denotes the different classes of the channels. The blur is due to measurement uncertainties. While the measurement uncertainty renders separable-state SVM inaccurate, the entanglement-enhanced SVM remains intact.

the measurement setting to minimize the error probability in producing a class label for the object. To this end, we introduce a variational circuit, implemented by a unitary operation $\hat{B}^\dagger(\mathbf{w})$ comprised of beam splitters and phase shifters [43], that acts on a resource squeezed vacuum state \hat{b}_1 with mean photon number N_S to generate the entangled probe state. A second variational circuit $\hat{B}(\mathbf{w})$ operates on the channel’s output entangled probe state \hat{a}'_n ’s to generate a single mode \hat{b}'_1 for detection. A homodyne measurement on \hat{b}'_1 yields outcome $f_{\mathbf{w}}(\Phi^{(n)})$. The intuition of such a design is that the expectation value of $f_{\mathbf{w}}(\Phi^{(n)})$ equals the weighted sum $\mathbf{w} \cdot \alpha^{(n)}$ (see Appendix A for details), which is exactly what Eq. 1 requires for SVM classification. Moreover, the multipartite entanglement suppresses the measurement uncertainties in analogy to the distributed sensing

scheme [30]. As such, a single measurement on the detection mode suffices. The two variational circuits are trained by a classical algorithm, as described below.

Training stage.— Without loss of generality, we first consider a binary classification problem. For a specific variational circuit setting \mathbf{w} , one generates a class label for the object as $\hat{y}^{(n)} = \text{sign}(f_{\mathbf{w}}(\Phi^{(n)}) + b)$, where b is tuned in classical post-processing. To train the variational circuits, N quantum channels $\Phi^{(n)}$, each labeled as $y^{(n)}$, are provided. The objective is to find the optimum SVM parameters \mathbf{w}^*, b^* to minimize the cost function defined by

$$\mathcal{E}_{\lambda}(\mathbf{w}, b) = \sum_{n=1}^N |1 - y^{(n)}(f_{\mathbf{w}}(\Phi^{(n)}) + b)|_+ + \lambda \|\mathbf{w}\|^2. \quad (2)$$

Here, $|x|_+$ equals x when $x \geq 0$ and zero otherwise, and $\|\cdot\|$ is a usual two-norm. The term $\lambda \|\mathbf{w}\|^2$ avoids over fitting. In this cost function, only the support vectors (SVs) — points close to the hyperplane described by \mathbf{w} and b with $y^{(n)}(\mathbf{w} \cdot \boldsymbol{\alpha}^{(n)} + b) \leq 1$ —non-trivially contribute to the cost function. The rationale behind the form of the cost function is that in a classification scenario errors mainly occurs on the SVs, thus introducing the deviation of all data points into the cost function is not ideal.

A typical method to minimize the cost function involves the use of the stochastic gradient descent algorithm [44]. However, for a general quantum circuit, an analytical form of the gradient is difficult to obtain due to the complexity associated with the measurement outcome $f_{\mathbf{w}}(\Phi^{(n)})$. Moreover, direct numerical estimate of the gradient requires a number of measurement-and-prepare steps proportional to the length of \mathbf{w} . To avoid the inefficiency, we use the simultaneous perturbation stochastic approximation (SPSA) method [45–47], which only needs to evaluate two points to simultaneously update the estimation of the function minimum and its gradient. With an updated \mathbf{w} , the transmissivities and phase shifts of the beam splitters in the two variational circuits are adjusted prior to the next training round, until the last training round yields \mathbf{w}^* and b^* .

Utilization stage.— Having obtained the optimum variational circuits parameterized by \mathbf{w}^*, b^* from training based on channels $\Phi^{(n)}$'s and their associated class labels $y^{(n)}$'s, we can now perform entanglement-enhanced classification on a new measurement outcome $f_{\mathbf{w}^*}(\Phi^{(N+1)})$ from an unknown quantum channel $\Phi^{(N+1)}$. To do so, we use the hyperplane described by \mathbf{w}^*, b^* to make a decision

$$\hat{y}^{(N+1)} = \text{sign}(f_{\mathbf{w}^*}(\Phi^{(N+1)}) + b^*). \quad (3)$$

By virtue of the reduced measurement error with the multipartite entanglement, a single measurement is sufficient for precise classification.

SVM simulations.— To compare the performance of the entanglement-enhanced SVM and separable-state SVM, we simulate the training process with N data

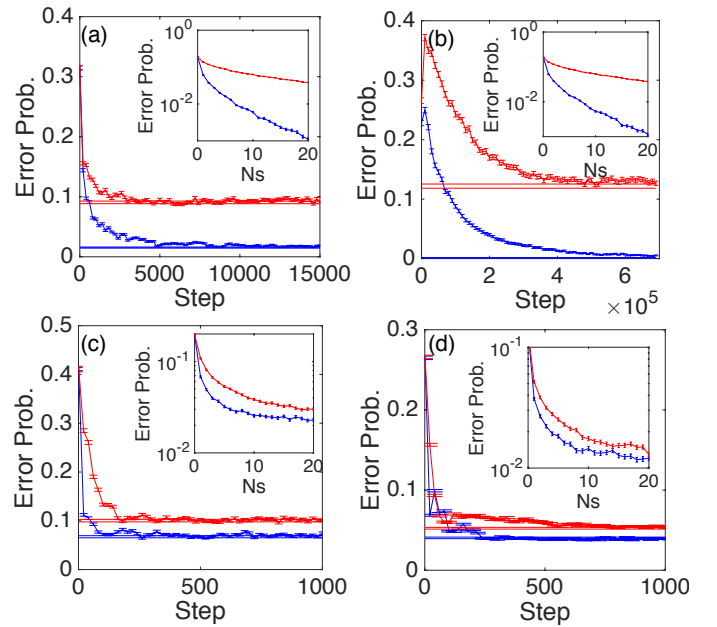


Figure 3. Training process and performance for SVM. Data points with error bars: performance of the SVM; Horizontal straight lines: the performance with the perfect hyperplane \mathbf{w}_t given, with \pm one standard deviation; Red plots: separable-state SVM; blue plots: entanglement-enhanced SVM. Insets: the scaling of the error probability of the optimum hyperplane with respect to the mean photon number N_s . (a) $\eta = 1$, $N_s = 5$, $\alpha_0 = 2$, $M = 10$. Number of data points $N = 10^3$, $\epsilon = 0.1$. (b) $\eta = 1$, $N_s = 20$, $\alpha_0 = 2$, $M = 100$. $N = 10^4$, $\epsilon = 0.1$. (c) $\eta = 0.9$, $N_s = 1$, $\alpha_0 = 1.5$, $M = 3$. $N = 500$. $\epsilon = 0.2$. (d) $\eta = 0.9$, $N_s = 1$, $\alpha_0 = 2$, $M = 2$. $N = 500$. $\epsilon = 0.2$. In each training step, the channel is randomly chosen from N data points and thus the total training steps can be larger than N .

points $(\boldsymbol{\alpha}^{(n)}, y^{(n)})$, $1 \leq n \leq N$. Each component $\alpha_m^{(n)}$, $1 \leq m \leq M$ of vector $\boldsymbol{\alpha}^{(n)}$ is randomly produced following a uniform distribution in $[-\alpha_0/2, \alpha_0/2]$. A random plane $y = \mathbf{w}_t \cdot \boldsymbol{\alpha}$ across the origin is subsequently generated, and true labels by $y^{(n)} = \text{sign}(\mathbf{w}_t \cdot \boldsymbol{\alpha}^{(n)})$ are assigned to each data point. To tune the difficulty of the problem, we exclude points within distance $\epsilon \geq 0$ to the hyperplane from the data set. Smaller ϵ means the SVs are closer to the hyperplane and thus the problem is more difficult. In the simulation, the measurement outcome is generated by Gaussian-distributed random numbers with mean of $\mathbf{w} \cdot \boldsymbol{\alpha}^{(n)}$ and variance given by Eqs. A2 and A3 in Appendix A for a symmetric case. Since the data are randomly generated, equally distributing the mean photon number of the squeezed state to different sensor nodes is optimum on average, thus we do not perform the costly optimization given by Eq. A3 for separable-state sensing. The achieved entanglement-enhanced advantage however holds for the most general case. Fig. 2 (bottom) provides a conceptual illustration of the performance contrast between entanglement-enhanced SVM and separable-state SVM (see caption for details).

To choose a proper regularization parameter λ to avoid over-fitting, we generate a test data set in the same way as the training data set. Since the performance is near identical for both data sets, we only show the training data result in the main plots of Fig. 3. The error probabilities of the SVM at different steps of the training process are plotted in connected points. To ensure convergence of the training process, we evaluate the performance of a perfect classifier with assigned surface $y = \mathbf{w}_t \cdot \boldsymbol{\alpha}$ in the horizontal solid lines. Due to the measurement uncertainty, even the perfect classifier suffers from a non-zero error probability. Both the entanglement-enhanced (blue) and separable-state (red) SVMs converge, but the entanglement-enhanced SVM enjoys an appreciable error-probability advantage.

We now address the error-probability scaling with respect to the resources, i.e., the number of sensors and the mean photon number of the resource squeezed state, employed in entanglement-enhanced SVM. The ultimate error probability is determined by the SVs ϵ -close to the hyperplane. For a given data set, we plot the error probability versus the mean photon number in the inset of Fig. 3. In the lossless cases, i.e., the transmissivity $\eta = 1$, the insets of Fig. 3 (a)(b) plot the error-probability contrast between the entanglement-enhanced SVM and separable-state SVM. The numerically computed error-probability is remnant of the analytically-derived error-probability scaling advantage for binary channel discrimination depicted in Fig. 7(b) in Appendix A.

In real applications, the minimum distance of the data points to the hyperplane ϵ scales with the data dimension, i.e., the number of sensors. In the usual case, each sensor measures a displacement of energy $\sim \epsilon_0^2$, thus the minimum distance scales as $\epsilon \simeq \sqrt{M}\epsilon_0$. The analysis in Appendix A, which agrees well with the presented numerical results, shows that for large N_S and M the error probability P_E for the entanglement-enhanced scheme with homodyne detection scales as $P_E \sim \exp(-2N_S M \epsilon_0^2)$, whereas the separate-state scheme has an error-probability scaling of $P_S \sim \exp(-4N_S \epsilon_0^2)$. This translates to an exponential error-probability advantage with respect to the data dimension, i.e., $P_E \sim P_S^{M/2}$. Such a enormous quantum advantage stems from the utilization of multipartite entanglement to directly extract a global feature of the object in a single-shot measurement, in contrast to the separate-state scheme's need for individual measurements on all local features.

In Fig. 3 (c)(d), we consider an entanglement-enhanced SVM with less mean photon number ($N_S = 1$) and number of sensors ($M = 2, 3$). We also include a pure loss channel with transmissivity $\eta = 0.9$ after each displacement unitary. These parameters represent an entanglement-enhanced SVM readily implementable in a bulk-optics platform. Remarkably, despite the saturation of the scaling advantage due to the presence of loss, as shown in the inset plots of Fig. 3 (c)(d), the entanglement-enhanced SVM's error-probability advantage survives the loss, demonstrating its tolerance to ex-

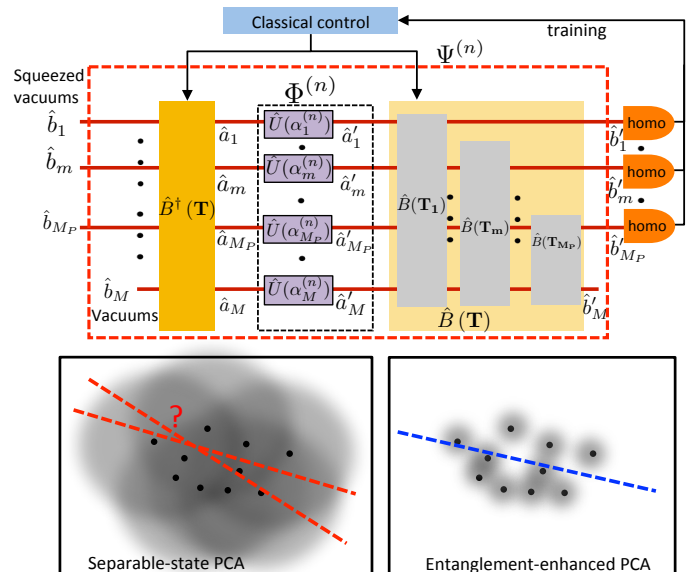


Figure 4. Top Panel: schematic of entanglement-enhanced principal component analyzer (PCA). The original channel $\Phi^{(n)}$ with dimension M is reduced to a new channel $\Psi^{(n)}$ with dimension M_P . The dimension reduction is carried out by two variational circuits, $\hat{B}(\mathbf{T})^\dagger$ and $\hat{B}(\mathbf{T})$ training by a classical algorithm. The training process requires M_P squeezed vacuum states at the input modes \hat{b}_1 to \hat{b}_{M_P} and M_P homodyne measurements at the output modes \hat{b}'_1 to \hat{b}'_{M_P} . Bottom panel: illustration of the performance contrast between the entanglement-enhanced PCA and separable-state PCA in the parameter space. The blur is due to measurement uncertainties. While the measurement uncertainties prevent the separable-state PCA from finding the principal axis, the entanglement-enhanced PCA precisely identifies the principal axis.

perimental imperfections.

IV. ENTANGLEMENT-ENHANCED PHYSICAL-LAYER PRINCIPAL-COMPONENT ANALYZER

Apart from entanglement-enhanced SVM, SLEEN can also be leveraged to construct an entanglement-enhanced physical-layer PCA as a powerful tool for dimensional reduction and quantum data compression. Utilized in SVM, for example, PCA is particularly useful for data dimension (i.e., the number of input and output modes of $\Phi^{(n)}$) reduction, so that the training of the optimum hyperplane for high-dimensional channels becomes viable (see Fig. 6). Given the classical description $\boldsymbol{\alpha}^{(n)} \in \mathbb{R}^M$ of $\Phi^{(n)}$, a classical PCA identifies the principal components (PCs) stored in a vector $\mathbf{c}^{(n)} \in \mathbb{R}^{M_P}$ with dimension $M_P \ll M$ through a linear transform $\mathbf{c}^{(n)} = \mathbf{T}\boldsymbol{\alpha}^{(n)}$, where $\mathbf{T} \in \mathbb{R}^{M_P \times M}$. These PCs are independent and form the large variance subspace of the original data set.

To avoid the inefficient channel tomography, we train a variational circuit to directly produce a reduced-

dimension channel $\Psi^{(n)}$ with M_P input modes and M_P output modes. $\Psi^{(n)}$ is described by the principal components $\mathbf{c}^{(n)}$. $\Psi^{(n)}$ is obtained by conjugating the original M -mode channel $\Phi^{(n)}$ with a beam-splitter array $\hat{B}(\mathbf{T})$, as illustrated in the red box of Fig. 4 (top). The construction of the variational circuit is similar to that for entanglement-enhanced SVM shown in Fig. 2 (top), except that the beam-splitter array for PCA requires the control of weights on M_P modes. The mode reduction is achieved by leaving the $M - M_P$ modes, \hat{b}_{M_P+1} to \hat{b}_M , in vacuum at the input and discarding $M - M_P$ modes, \hat{b}'_{M_P+1} to \hat{b}'_M , at the output. Due to the conjugation relation of the two beam splitters, the new channel $\Psi^{(n)}$ remains unitary in the absence of extra loss.

Training stage.— To train the variational circuits, squeezed vacuum states are injected at the M_P input modes of the channel $\Psi^{(n)}$. A homodyne measurement is performed on each of the M_P output modes, yielding joint measurement outcomes $f_{\mathbf{T}}(\Phi^{(n)}) \in \mathbb{R}^{M_P}$. Since precise knowledge of $\Phi^{(n)}$ is unavailable, we use the gradient-free SPSA method, in lieu of the gradient descent approach [48], to maximize $\|f_{\mathbf{T}}(\Phi^{(n)})\|^2$ by tuning the beam-splitter array parameter \mathbf{T} based on the measurement outcome. As shown in Fig. 4, the training process can be performed in a sequential order: the variational circuit is decomposed into $\hat{B}(\mathbf{T}) = \hat{B}(\mathbf{T}_1) \circ \hat{B}(\mathbf{T}_2) \circ \dots \circ \hat{B}(\mathbf{T}_m) \circ \dots \circ \hat{B}(\mathbf{T}_{M_P})$. In doing so, each transform $\hat{B}(\mathbf{T}_m)$ only takes the m th to M th modes as its input. In the m th step, one maximizes the measurement variance of mode \hat{b}'_m by solely tuning $\hat{B}(\mathbf{T}_m)$, with the previous optimized beam-splitter arrays $\hat{B}(\mathbf{T}_1^*) \circ \dots \circ \hat{B}(\mathbf{T}_{m-1}^*)$ unchanged. Executing the process from $m = 1$ to $m = M_P$, one obtains the optimum transform \mathbf{T}^* to produce $\Psi^{(n)}$ characterized by the PCs.

Utilization stage.— The training yields the optimum variational circuits parameterized by \mathbf{T}^* . To use the entanglement-enhanced PCA, $\hat{B}^{\dagger}(\mathbf{T}^*)$ is applied on the M input modes of the channel $\Phi^{(N+1)}$, and $\hat{B}(\mathbf{T}^*)$ is applied on its M output modes. This results in a reduced-dimension effective channel with M_P modes at both the input and output.

The reduced-dimensional channel can in turn be used in other SL tasks. Fig. 6 provides an example: the entanglement-enhanced PCA is utilized as the pre-processor of the entanglement-enhanced SVM. Given an M -mode channel $\Phi^{(n)}$, prior to utilizing the entanglement-enhanced SVM, one first reduces its dimension to an M_P -mode channel $\Psi^{(n)}$ by the entanglement-enhanced PCA, as illustrated by the components in the red dashed rectangle. In doing so, the SVM only needs to process a reduced-dimension channel $\Psi^{(n)}$, thus leading to a significant speedup in training the SVM.

PCA simulations.— We demonstrate the training of the first variational circuit, the beam-splitter array $\hat{B}(\mathbf{T}_1)$, to obtain the reduced-dimension channel associated with the first PC. The training only needs a single-mode squeezed vacuum state with mean photon number

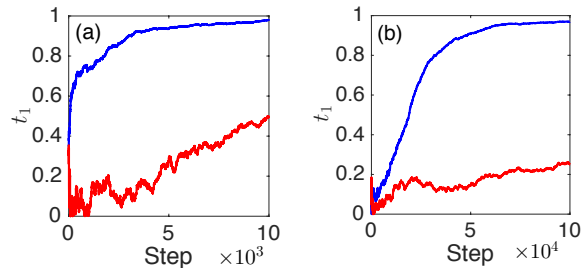


Figure 5. Training process of the entanglement-enhanced PCA. Blue plots: performance of entanglement-enhanced PCA; red plots: the performance of separable-state PCA. (a) $M = 20$, $N_S = 1$, $\alpha_0 = 0.3$, $P = 20$. (b) $M = 100$, $N_S = 1$, $\alpha_0 = 0.4$, $P = 100$.

N_S at the input. We randomly generate channels $\Phi^{(n)}$ with zero-mean Gaussian-distributed $\alpha^{(n)}$'s and simulate the quantum noise in the measurement outcome. We set the covariance matrix to $\alpha_0^2 \text{Diag}[P, 1, 1, \dots, 1]$ with $P > 1$, thus the true PC is obtained by the transform $\mathbf{T}_1^* = [1, 0, 0, \dots, 0]$. Since we initialize the parameters \mathbf{T}_1 randomly, a diagonal covariance matrix is general. We plot the first element t_1 of the normalized vector \mathbf{T}_1 during training and compare it with \mathbf{T}_1^* . Similar to what has been done in the entanglement-enhanced SVM, we compare the performance of the entanglement-enhanced PCA (blue) with the optimum separable-state PCA (red) in Fig. 5. The result shows that while the separable-state PCA struggles to find the PC, the entanglement-enhanced PCA converges very close to the actual PC. This is because vacuum noise dominates the measurements in separable-state PCA due to a small variance of α_0^2 , leading to a close to symmetric variances over all modes. In contrast, the entanglement-enhanced PCA leverages the multipartite entanglement to reduce the vacuum noise and thus is able to obtain the correct PC. Fig. 4 (bottom) conceptually illustrates that entanglement-enhanced PCA is able to solve classically intractable problems.

V. DISCUSSIONS

In this paper, we utilize SLEEN to construct the entanglement-enhanced SVM and PCA. SLEEN only requires off-the-shelf components and are robust against noise, thus representing a paradigm for demonstrating a practical quantum advantage in near-term devices. SLEEN measures field-quadrature displacements, but it can be generalized to cope with other displacements on canonical conjugate variables including time and frequency, angular momentum and angle, and number and phase.

Our entanglement-enhanced SVM opens new avenues for ultrasensitive measurements in biological, thermal, and mechanical systems. A key ingredient for the

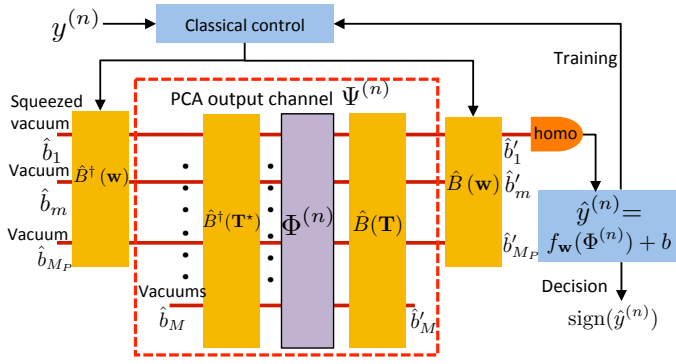


Figure 6. A combined scheme with entanglement-enhanced SVM and PCA. Using multipartite entangled probe states, the PCA is training to reduce the original M -mode quantum channel $\Phi^{(n)}$ (purple rectangle) to a M_P -mode quantum channel $\Psi^{(n)}$ (red dashed box), which is in turn used by the entanglement-enhanced SVM to carry out data classification tasks.

entanglement-enhanced SVM is transducers that convert the information carried on the samples into phase modulation. For example, electro-optic devices can convert radio-frequency (RF) signals into refractive index shift of optical materials, which in turn impart phase modulation on light [18]. In optical biosensors, the evanescent wave of the probe light interacts with the sample, and the induced phase shift serves as a means to identify the density and species of the bio-molecule [19]. These phase shifts, in turn can be transformed into displacement through a Mach-Zehnder interferometer (see Fig. 8 in Appendix C), where for the single-mode case squeezed state is known to be beneficial [20, 21]. In such a scenario, the entanglement-enhanced SVM enables much more efficient and sensitive classification on data acquired by phase sensing than what sensors based on classical light can afford.

In the given sensing examples, the transducers can be engineered to introduce nonlinearity when converting the physical parameters being probed into phase modulation on the entangled photons. In RF sensing, the intrinsic nonlinearity of the electro-optic devices can be leveraged. Likewise, by properly designing the waveguide geometry, the phase shift induced by optical biosensors can be engineered to be nonlinearly dependent on the density of the bio-molecules. The introduced measurement nonlinearity would be a key to implement entanglement-enhanced general-kernel SVM.

Before closing, we point out that the proposed entanglement-enhanced SVM applies in a very different scenarios than existing proposals for quantum SVMs [49]. By transforming the SVM cost function to a quadratic form [50], quantum speedup is claimed with mechanisms similar to a linear system of equations, assuming qRAMs are available. However, more recent studies of quantum-inspired classical algorithms show that such speedups are in fact questionable for various cases [51–53]. Moreover,

due to the channel noise, such a quantum SVM algorithms is not directly applicable to our channel learning problems.

A few future developments for SLEEN would make it more widely applicable. First, the binary-hypothesis entanglement-enhanced SVM can be generalized to a multi-hypothesis SVM by introducing a series of binary classification tasks [54, 55] or by adding multiple hyperplanes [56]. The current SLEEN architecture can be adapted to accommodate either case. Second, introducing nonlinear maps into SLEEN would make it capable of dealing with nonlinear data classification and compression problems. Third, an extension of the CV sensing scheme to incorporate DV sensing of phase rotations is another interesting open problem. Ref. [57] presents a proposal for measuring a weighted average through controlling the integration time on each qubit. It is open whether there are ways of implementing the measurement for given fixed unitary phase rotations. While direct measurements of a weighted average appears difficult, classification without resorting to direct intuitions has been considered [10–13].

ACKNOWLEDGMENTS

We thank helpful discussions with Jeffrey Shapiro, Umesh Vazirani and Zeph Landau. Q.Z. and Z.Z. are grateful for the support from the University of Arizona. Q.Z. acknowledges the U.S. Department of Energy through Grant No. PH-COMPHEP-KA24.

Appendix A: Entangled sensor network for channel discrimination

A key component in the CV distributed sensing scheme [30] is an interferometer structure formed by two beam-splitter arrays. By conjugating an array of displacement unitaries with a suitable beam-splitter unitary \hat{B} (see Fig. 7(a)), we can mix the amplitudes of displacements:

$$\hat{B}^\dagger \left(\otimes_{m=1}^M \hat{U}(\alpha_m) \right) \hat{B} = \hat{U}(\tilde{\alpha}) \otimes \left(\otimes_{\ell=2}^M \hat{U}(\alpha'_m) \right), \quad (\text{A1})$$

where $\tilde{\alpha} = \sum_m w_m \alpha_m$ is the effective displacement between modes \hat{b}_1 and \hat{b}'_1 . The weights w_m 's are normalized, i.e., $\sum_{m=1}^M w_m^2 = 1$. Note that an arbitrary choice of weights w_m 's only requires M two-mode beam splitters to realize. Suppose we use a squeezed vacuum state with squeezing parameter r at mode \hat{b}_1 as the input, then we can measure $\tilde{\alpha}$ more precisely on mode \hat{b}'_1 . In this way, the input modes $\hat{a}_1, \dots, \hat{a}_M$ to the displacement channel are in fact entangled. The original entanglement-enhanced distributed sensing scheme measures the weighted average $\omega \cdot \alpha^{(n)}$ in presence of a detection loss η to a precision

$$\delta \alpha_\eta^E = (\eta g (N_S) + 1 - \eta)^{1/2} / 2, \quad (\text{A2})$$

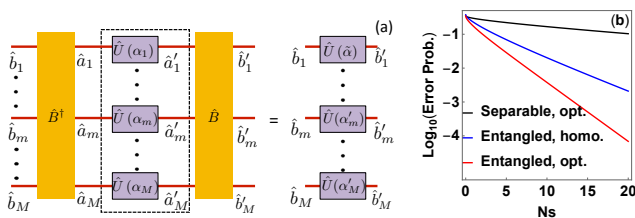


Figure 7. (a) Interferometer structure for amplitude mixing in a distributed sensing scheme. (b) Performance of the symmetric case, $M = 10$ and $\alpha_m = 0.1, 1 \leq m \leq M$.

where $g(n) \equiv 1/(\sqrt{n+1} + \sqrt{n})^2$ and N_S is the total mean photon number; while a scheme using separable squeezed states for modes $\hat{a}_1, \dots, \hat{a}_M$ has precision given by a constrained optimization,

$$\delta\alpha_\eta^P = \min_{\sum_{m=1}^M N_m = N_S} \left[\eta \sum_{m=1}^M (w_m^2 g(N_m)) + 1 - \eta \right]^{1/2}, \quad (\text{A3})$$

with the total mean photon number N_S as a constraint. In the lossless case, one can prove that the above entangled scheme is optimum among all schemes and the above separable scheme is also optimum among all schemes without using entanglement [58]. Moreover, in the lossy case, the optimality of both schemes still holds when we restrict the probe states to be Gaussian [30]. For the equal weight case, the minimum $\delta\alpha_\eta^P$ is obtained by setting $N_m = N_S/M, 1 \leq m \leq M$ in Eq. A3. As shown in Ref. [30], when the mean photon number per mode N_S/M is fixed, in the lossless case ($\eta = 1$) the entangled scheme has a Heisenberg-scaling precision ($\delta\alpha_\eta^E \sim 1/M$), while the separable-state scheme obeys the standard quantum limit ($\delta\alpha_\eta^P \sim 1/\sqrt{M}$). Moreover, despite that the Heisenberg scaling is destroyed by loss ($\eta < 1$), the advantage vouchsafed by entanglement survives.

To understand how the above advantage translates to channel-classification problems, we calculate the error probability performance of a simple binary channel discrimination task between displacements $\{\mathbf{0}, \boldsymbol{\alpha}\}$ with given prior probabilities $\{\pi_0, \pi_1\}$ in the lossless ($\eta = 1$) case. For the case of $\mathbf{0}$, the transformed displacements are all zero regardless of the beam splitters choice. For the case of $\boldsymbol{\alpha}$, we have $\tilde{\alpha} = \|\boldsymbol{\alpha}\|$ while all other displacements are zero, by choosing the beam-splitter array in Fig. 7(a) to have $w_m = \alpha_m/\|\boldsymbol{\alpha}\|$. This can always be ensured as follows. First, one performs a beam-splitter transform between \hat{b}_1 and \hat{b}_2 to produce the mode $\frac{\alpha_1}{\sqrt{\alpha_1^2 + \alpha_2^2}}\hat{b}_1 + \frac{\alpha_2}{\sqrt{\alpha_1^2 + \alpha_2^2}}\hat{b}_2$. Afterwards, one performs another beam-splitter transform on the previous output mode and $\hat{b}_3, \dots, \hat{b}_M$. Since beam splitters conserve the mean photon number and the effective displacement on \hat{b}_1 is $\|\boldsymbol{\alpha}\|$, all the other effective displacements are zero.

In this way, the multi-mode problem is reduced to

a single-mode problem of determining whether a displacement unitary has amplitude zero or $\|\boldsymbol{\alpha}\|$. In Appendix B, we show that the optimum input Gaussian state that minimizes the Helstrom limit [33] is a single-mode squeezed vacuum state and the corresponding error probability is

$$P_{\{\pi_0, \pi_1\}}^E = \left[1 - \sqrt{1 - 4\pi_0\pi_1 \exp(-e^{2r}\|\boldsymbol{\alpha}\|^2)} \right] / 2 \simeq \pi_0\pi_1 \exp(-e^{2r}\|\boldsymbol{\alpha}\|^2), \quad (\text{A4})$$

where $\sinh^2(r) = N_S$ is the mean photon number. Thus, in terms of the error probability, the considered entangled scheme is the optimum and the considered separable-state scheme is the optimum among all Gaussian schemes without using entanglement. In general, non-Gaussian inputs may lead to better performances, but the advantage of an entanglement-enhanced sensing scheme still holds.

Having obtained the optimum Gaussian input state that minimizes the Helstrom limit, now we derive the corresponding measurement scheme to achieve the Helstrom limit. The construction is as follows. First, one performs a squeezing of amplitude $-r$ on \hat{b}'_1 to obtain the coherent state $|e^r\|\boldsymbol{\alpha}\|\rangle$ or $|0\rangle$; Next, one applies a slicing Dolinar receiver [59] scheme on the output. The optimality of the above scheme simply follows from the optimality of the Dolinar receiver. However, this construction requires feed-forward and photon number counting. A more practical scheme is to perform a homodyne detection with a maximum-likelihood decision rule, where the error probability can be evaluated by the Gaussian error function. For the $\pi_1 = \pi_0 = 1/2$ case, the formula is simple,

$$P_{\{1/2, 1/2\}}^{E, Het} = \frac{1}{2} \text{Erfc} \left[\frac{\|\boldsymbol{\alpha}\|}{\sqrt{2}e^{-r}} \right] \sim \exp[-e^{2r}\|\boldsymbol{\alpha}\|^2/2]. \quad (\text{A5})$$

Comparing to Eq. A4, it is only a factor of two worse in the error exponent in the asymptotic limit.

Now we compare the performance of the entangled scheme with the optimum Gaussian separable-state scheme. To ensure a fair comparison, we set the total mean photon number to be $N_S = \sum_{m=1}^M N_m$, where $N_m \equiv \sinh^2(r_m)$ is the mean photon number of the input to the m th displacement. Given the constraint on the mean photon number N_m , for each mode a single-mode squeezed state is the optimum Gaussian input state, thus to minimize the Helstrom limit, one needs to optimize the distribution of mean photon number to minimize the overlap $|\langle \psi_0^M | \psi_1^M \rangle|^2 = \exp(-\sum_{m=1}^M e^{2r_m} \alpha_m^2)$, where $\psi_k^M, k = 0, 1$ are the M -mode joint output states in each hypothesis. Given the minimum E_{\min} of $|\langle \psi_0^M | \psi_1^M \rangle|^2$, the Helstrom limit of the error probability is $P_{\pi_0, \pi_1}^S = \frac{1}{2} [1 - \sqrt{1 - 4\pi_0\pi_1 E_{\min}}]$. In general, there is no closed form solution. Because e^{2r_m} , as a function of N_m , is concave, so for equal α_m 's it is optimum to evenly distribute the photons. Moreover, for large N_S 's concentrating most photon number on the mode with the largest α_m

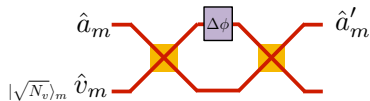


Figure 8. Schematic of conversion between phase shift and displacement through a Mach-Zehnder interferometer.

is close to the optimum.

From the above analysis, we see the entanglement-enhanced scheme is strictly better than the separable-state scheme. The advantage is the most significant under $\sum_{m=1}^M \alpha_m^2 \gg \max_{1 \leq m \leq M} \alpha_m^2$. Asymptotically, for a fixed M , a large N_S , and $\alpha = (\alpha, \dots, \alpha)$, the error exponents for the separable-state scheme, the entanglement-enhanced scheme with homodyne measurements, and the entanglement-enhanced scheme with the optimum measurements are $4N_S\alpha^2$, $2N_S M\alpha^2$, and $4N_S M\alpha^2$. This shows a substantial advantage for large M 's. We give a numerical example in Fig. 7(b) for a moderate size $M = 10$ and show that the advantage is already appreciable.

Appendix B: Optimum Gaussian state for single-mode displacement discrimination

Now we consider the single-mode channel discrimination problem of two displacement operators $\hat{U}(0)$ and $\hat{U}(\alpha)$. We show that the input Gaussian state that minimizes the Helstrom limit of the error probability is the single-mode squeezed vacuum state.

We first consider an input mode entangled with an ancilla mode. Due to the ancilla, it suffices to consider an input-ancilla joint pure state $|\psi\rangle$. Then in each hypothesis we have the output state $|\psi_0\rangle = |\psi\rangle$ and $|\psi_1\rangle = \hat{U}(\alpha) \otimes \hat{I} |\psi\rangle$. Given the prior probabilities $\pi_0, \pi_1 = 1 - \pi_0$, the minimum error probability in the discrimination of the two outputs is given by the Helstrom limit

$$P_{\{\pi_0, \pi_1\}}(\psi_0, \psi_1) = \frac{1}{2} \left[1 - \sqrt{1 - 4\pi_0\pi_1 |\langle \psi_0 | \psi_1 \rangle|^2} \right]. \quad (\text{B1})$$

Thus we aim to minimize $|\langle \psi_0 | \psi_1 \rangle|^2 = |\langle \psi | (\hat{U}(\alpha) \otimes \hat{I}) | \psi \rangle|^2$, subject to certain constraints on

the input state $|\psi\rangle$.

While the optimization is in general difficult, we can optimize over Gaussian states to obtain the optimum Gaussian input. For pure two-mode Gaussian states with the covariance matrix V and mean $\mu_0 = (0, 0, 0, 0)$ and $\mu_1 = (2\alpha, 0, 0, 0)$, the overlap is [60]

$$|\langle \psi_0 | \psi_1 \rangle|^2 = \exp \left[-\frac{1}{4} (\mu_1 - \mu_0)^T V^{-1} (\mu_1 - \mu_0) \right]. \quad (\text{B2})$$

The above equation indicates that minimizing the state overlap is equivalent to minimizing the variance of the first quadrature, as expected from intuition.

The resource in our task is the mean photon number of the first mode. Given the uncertainty principle $\delta^2 q \cdot \delta^2 p \geq 1$ and energy constraint $\delta^2 q + \delta^2 p \leq N_S$, we conclude that it is optimum to use a single-mode squeezed vacuum, without requiring entanglement assistance. Thus, the optimum general Gaussian state for single-mode displacement discrimination is a single-mode squeezed vacuum state.

The corresponding error probability can be obtained, based on the covariance matrix $V = \text{Diag}[e^{-2r}, e^{2r}, 1, 1]$ and the total mean photon number constraint $N_S = \sinh^2(r)$, as

$$P_{\{\pi_0, \pi_1\}} = \frac{1}{2} \left[1 - \sqrt{1 - 4\pi_0\pi_1 \exp(-e^{2r}\alpha^2)} \right] \simeq \pi_0\pi_1 \exp(-e^{2r}\alpha^2). \quad (\text{B3})$$

Appendix C: Conversion between displacement sensing and phase sensing

It suffices to illustrate the displacement-phase conversion using a single-mode case in Fig. 8. Consider a phase shift $\Delta\phi \ll 1$. When sandwiched between two beam splitters, with one of the input mode \hat{v}_m in a coherent state $|\sqrt{N_v}\rangle_m$, the phase shift leads to a mode transform (to the first order) as

$$\hat{a}'_m = (1 - i\Delta\phi/2)\hat{a}_m + i\hat{v}_m\Delta\phi/2, \quad (\text{C1})$$

where $\Delta\phi$ is embedded in a field-quadrature displacement $\alpha = i\sqrt{N_v}\Delta\phi/2$ of \hat{a}'_m . To generalize, when a sensor array measures multiple spatiotemporal phase shifts, the output signals will be in a form of multimode displacement.

-
- [1] “The future is quantum,” <https://www.ibm.com/blogs/research/2017/11/the-future-is-quantum/> (2017), [Online; accessed 26-November-2018].
- [2] D. Castelvecchi, *Nature News* **541**, 9 (2017).
- [3] J. Preskill, *Quantum* **2**, 79 (2018).
- [4] S. Bravyi, D. Gosset, and R. Koenig, *Science* **362**, 308 (2018).

- [5] A. Bouland, B. Fefferman, C. Nirkhe, and U. Vazirani, *Nat. Phys.* **1** (2018).
- [6] D. Wecker, M. B. Hastings, and M. Troyer, *Phys. Rev. A* **92**, 042303 (2015).
- [7] A. Peruzzo, J. McClean, P. Shadbolt, M.-H. Yung, X.-Q. Zhou, P. J. Love, A. Aspuru-Guzik, and J. L. O’Brien, *Nat. Commun.* **5**, 4213 (2014).

- [8] A. Kandala, A. Mezzacapo, K. Temme, M. Takita, M. Brink, J. M. Chow, and J. M. Gambetta, *Nature* **549**, 242 (2017).
- [9] R. LaRose, A. Tikku, É. O’Neel-Judy, L. Cincio, and P. J. Coles, arXiv:1810.10506 (2018).
- [10] V. Havlicek, A. D. Córcoles, K. Temme, A. W. Harrow, J. M. Chow, and J. M. Gambetta, arXiv:1804.11326 (2018).
- [11] M. Schuld and N. Killoran, arXiv:1803.07128 (2018).
- [12] J. Biamonte, P. Wittek, N. Pancotti, P. Rebentrost, N. Wiebe, and S. Lloyd, *Nature* **549**, 195 (2017).
- [13] V. Dunjko and H. J. Briegel, *Rep. Prog. Phys.* **81**, 074001 (2018).
- [14] N. Killoran, T. R. Bromley, J. M. Arrazola, M. Schuld, N. Quesada, and S. Lloyd, arXiv:1806.06871 (2018).
- [15] S. Arunachalam, V. Gheorghiu, T. Jochym-O’Connor, M. Mosca, and P. V. Srinivasan, *New J. Phys.* **17**, 123010 (2015).
- [16] K. Eckert, O. Romero-Isart, M. Rodriguez, M. Lewenstein, E. S. Polzik, and A. Sanpera, *Nat. Phys.* **4**, 50 (2008).
- [17] M. Mehboudi, M. Moreno-Cardoner, G. De Chiara, and A. Sanpera, *New J. Phys.* **17**, 055020 (2015).
- [18] L. Fan, C.-L. Zou, R. Cheng, X. Guo, X. Han, Z. Gong, S. Wang, and H. X. Tang, arXiv:1805.04509 (2018).
- [19] A. Fernández Gavela, D. Grajales García, J. Ramirez, and L. Lechuga, *Sensors* **16**, 285 (2016).
- [20] B. Escher, R. de Matos Filho, and L. Davidovich, *Nat. Phys.* **7**, 406 (2011).
- [21] R. Demkowicz-Dobrzański, K. Banaszek, and R. Schnabel, *Phys. Rev. A* **88**, 041802 (2013).
- [22] V. Giovannetti, S. Lloyd, and L. Maccone, *Phys. Rev. Lett.* **96**, 010401 (2006).
- [23] V. Giovannetti, S. Lloyd, and L. Maccone, *Nat. Photonics* **5**, 222 (2011).
- [24] S. Pirandola, B. R. Bardhan, T. Gehring, C. Weedbrook, and S. Lloyd, *Nat. Photonics* **12**, 724 (2018).
- [25] F. Caruso, V. Giovannetti, C. Lupo, and S. Mancini, *Rev. Mod. Phys.* **86**, 1203 (2014).
- [26] S.-H. Tan, B. I. Erkmen, V. Giovannetti, S. Guha, S. Lloyd, L. Maccone, S. Pirandola, and J. H. Shapiro, *Phys. Rev. Lett.* **101**, 253601 (2008).
- [27] W. Denk, J. H. Strickler, and W. W. Webb, *Science* **248**, 73 (1990).
- [28] A. Eshun, Z. Cai, M. Awies, L. Yu, and T. Goodson III, *J. Phys. Chem. A* **122**, 8167 (2018).
- [29] S. Pirandola, *Phys. Rev. Lett.* **106**, 090504 (2011).
- [30] Q. Zhuang, Z. Zhang, and J. H. Shapiro, *Phys. Rev. A* **97**, 032329 (2018).
- [31] J. Maze, P. Stanwix, J. Hodges, S. Hong, J. Taylor, P. Cappellaro, L. Jiang, M. G. Dutt, E. Togan, A. Zibrov, *et al.*, *Nature* **455**, 644 (2008).
- [32] R. Bergh, H. Lefevre, and H. Shaw, *Opt. Lett.* **6**, 502 (1981).
- [33] C. Helstrom, *Quantum Detection and Estimation Theory*, Mathematics in Science and Engineering : a series of monographs and textbooks (Academic Press, 1976).
- [34] A. Holevo, *Probabilistic and Statistical Aspects of Quantum Mechanics* (North-Holland, Amsterdam, 1982).
- [35] H. Yuen and M. Lax, *IEEE Trans. Inf. Theory* **19**, 740 (1973).
- [36] W. Ge, K. Jacobs, Z. Eldredge, A. V. Gorshkov, and M. Foss-Feig, *Phys. Rev. Lett.* **121**, 043604 (2018).
- [37] T. J. Proctor, P. A. Knott, and J. A. Dunningham, *Phys. Rev. Lett.* **120**, 080501 (2018).
- [38] V. Giovannetti, S. Lloyd, and L. Maccone, *Nature* **412**, 417 (2001).
- [39] V. Giovannetti, S. Lloyd, and L. Maccone, *Science* **306**, 1330 (2004).
- [40] B. Escher, R. de Matos Filho, and L. Davidovich, *Nat. Phys.* **7**, 406 (2011).
- [41] Q. Zhuang, Z. Zhang, and J. H. Shapiro, *Phys. Rev. A* **96**, 040304 (2017).
- [42] C. Cortes and V. Vapnik, *Machine learning* **20**, 273 (1995).
- [43] C. Weedbrook, S. Pirandola, R. García-Patrón, N. J. Cerf, T. C. Ralph, J. H. Shapiro, and S. Lloyd, *Rev. Mod. Phys.* **84**, 621 (2012).
- [44] L. Rosasco and T. Poggio, “Machine learning: A regularization approach,” (2015).
- [45] J. C. Spall, *IEEE Trans. Autom. Control* **45**, 1839 (2000).
- [46] J. C. Spall, *IEEE Trans. Aerosp. Electron. Syst.* **34**, 817 (1998).
- [47] “Simultaneous perturbation stochastic approximation—a method for system optimization,” <https://www.jhuapl.edu/SPSA/#Overview> (2001), [Online; accessed 26-November-2018].
- [48] O. Shamir, in *ICML* (2016) pp. 257–265.
- [49] P. Rebentrost, M. Mohseni, and S. Lloyd, *Phys. Rev. Lett.* **113**, 130503 (2014).
- [50] J. A. Suykens and J. Vandewalle, *Neural Process. Lett.* **9**, 293 (1999).
- [51] A. Gilyén, S. Lloyd, and E. Tang, arXiv:1811.04909 (2018).
- [52] E. Tang, arXiv:1807.04271 (2018).
- [53] E. Tang, arXiv:1811.00414 (2018).
- [54] R. Rifkin and A. Klautau, *Journal of machine learning research* **5**, 101 (2004).
- [55] S.-H. Park and J. Fürnkranz, in *European Conference on Machine Learning* (Springer, 2007) pp. 658–665.
- [56] J. Weston, C. Watkins, *et al.*, in *Esann*, Vol. 99 (1999) pp. 219–224.
- [57] Z. Eldredge, M. Foss-Feig, J. A. Gross, S. L. Rolston, and A. V. Gorshkov, *Phys. Rev. A* **97**, 042337 (2018).
- [58] Y. Xia, Q. Zhuang, W. Clark, and Z. Zhang, *Phys. Rev. A* **99**, 012328 (2019).
- [59] S. J. Dolinar, *Processing and Transmission of Information*, Technical Report (RLE MIT, 1973).
- [60] P. Marian and T. A. Marian, *Phys. Rev. A* **93**, 052330 (2016).